Histochem Cell Biol (2013) 139:391–402
DOI 10.1007/s00418-012-1068-3

ORIGINAL PAPER

A novel method for quantified, superresolved, three-dimensional colocalisation of isotropic, fluorescent particles

Boguslaw Obara · Asma Jabeen · Nelson Fernandez · Pierre Philippe Laissue

Accepted: 27 November 2012 / Published online: 5 February 2013

Abstract Colocalisation, the overlap of subcellular structures labelled with different colours, is a key step to characterise cellular phenotypes. We have developed a novel bioimage informatics approach for quantifying colocalisation of round, blob-like structures in two-colour, highly resolved, three-dimensional fluorescence microscopy datasets. First, the algorithm identifies isotropic fluorescent particles, of relative brightness compared to their immediate neighbourhood, in three dimensions and for each colour. The centroids of these spots are then determined, and each object in one location of a colour image is checked for a corresponding object in the other colour image. Three-dimensional distance maps between the centroids of differently coloured spots then display where and how closely they colocalise, while histograms allow to analyse all colocalisation distances. We use the method to reveal sparse colocalisation of different human leukocyte antigen receptors in choriocarcinoma cells. It can also be applied to other isotropic subcellular structures such as vesicles, aggresomes and chloroplasts. The simple, robust and fast approach yields superresolved, object-based colocalisation maps and provides a first indication of protein–protein interactions of fluorescent, isotropic particles.

Keywords Colocalisation · Quantification · Superresolution · Confocal microscopy · Surface receptors · Bioimage informatics

Abbreviations

2D	Two-dimensional
3D	Three-dimensional
AU	Arbitrary unit
DAPI	4′,6-Diamidino-2-phenylindole
FRET	Förster resonance energy transfer
GUI	Graphical User Interface
HLA	Human leukocyte antigen
LoG	Laplace of Gaussian
MHC	Major histocompatibility class
PMT	Photomultiplier tube
PSF	Point spread function
SNR	Signal-to-noise ratio
LUT	Look-up table

Introduction

Modern cell biology relies on fluorescence microscopy to assess the distribution and potential roles of cellular proteins. As many research labs produce more and larger datasets daily, there is a need for quantified, automated

Electronic supplementary material The online version of this article (doi:10.1007/s00418-012-1068-3) contains supplementary material, which is available to authorized users.

B. Obara (✉)
School of Engineering and Computing Sciences, University of Durham, Durham DH1 3LE, UK
e-mail: boguslaw.obara@durham.ac.uk

B. Obara
Oxford Centre for Integrative Systems Biology, University of Oxford, Oxford OX1 3QG, UK

B. Obara
Oxford e-Research Centre, University of Oxford, Oxford OX1 3QG, UK

A. Jabeen · N. Fernandez · P. P. Laissue (✉)
School of Biological Sciences, University of Essex, Colchester CO4 3SQ, UK
e-mail: plaissue@essex.ac.uk

image analysis to characterise cellular phenotypes (Verveer and Bastiaens 2008). This allows not only the assessment of clear differences between individual phenotypes and timepoints but also the discovery of subtle changes that are not obvious to an observer by visual inspection. Colocalisation, i.e. overlap between two or more differently labelled structures, is an important step for cellular phenotyping (Bolte and Cordelières 2006; Zinchuk et al. 2007). It allows to detect the overlap of one protein, labelled with a fluorophore, with another protein, tagged with a fluorophore emitting at a different wavelength. This is often assessed qualitatively. For instance, overlaid images from a green and a red channel show overlapping regions as yellow and are classified as 'colocalising'. Such impressions can, however, be misleading as the hue depends on the contrast adjustment in each channel, as well as on the calibration of the display equipment. For a quantitative analysis of colocalisation, statistical methods exist to determine the overlap globally, i.e. in the entire image, on a pixel-per-pixel basis. The correlation coefficients of Pearson (Manders et al. 1992; Press et al. 1992) or Manders et al. (1993) are commonly chosen as indicators for high degrees of correlation or anti-correlation. Alternative advanced intensity-based correlation coefficients have been introduced (Costes et al. 2004; Li et al. 2004). But when the degree of colocalisation is low, these indicators are difficult to interpret. For such cases, a better approach is to look at the overlap of only the pixels representing specific structures, or objects, rather than all pixels making up the whole image. Such object-based colocalisation requires first that objects are identified and separated from surrounding parts of the image. Then, each object in one location of a colour channel is checked for a corresponding object in the other colour channel. If they are close together, their degree of overlap is determined, resulting in quantitative, object-based colocalisation.

An individual protein or a small cluster of proteins is in most cases too small to be resolved by conventional widefield or confocal fluorescence microscopy. The image of such a punctate cellular structure will appear as a round (isotropic), blurred, diffraction-limited spot (in 2D [*xy*]) or ellipsoid (in 3D [*xyz*]), with the highest fluorescent intensity at its centre, as the point spread function (PSF, determined by the microscope setup) convolves with the object (the labelled surface receptor) to produce the image. In image processing, such a rounded region of interest, with a higher contrast compared to its local background, is referred to as blob-like object (as opposed to tube- or cloud-shaped objects). It is possible to determine the centre of such individual blobs with subpixel-accuracy, resulting in subdiffraction resolution. As the pattern of the PSF is a computationally demanding Bessel function, it can be approximated in easier ways, for example by fitting a Gaussian function and determining the centroid.

A Gaussian function-based approach has been proposed by Anderson et al. (1992) and updated by Morrison et al. (2003). Here, each source of fluorescence is localised by fitting a Gaussian distribution to the local window with the least-squares method (Marquardt 1963). The local window position can be calculated by detecting local maxima in the image using a non-maximum suppression algorithm (Wolter et al. 2010). The degree of colocalisation for correlated spots in two analysed images can then be quantified by the overlap integral (Morrison et al. 2003), which represents the volume shared by two 2D-Gaussian shapes, or by applying coordinate-based algorithms (Malkusch et al. 2012). However, these approaches are not 3D, require a small window size to minimise neighbourhood interference from non-uniform background levels, and use a rectangular rather than a circular structuring element to detect spots. Bypassing these limitations, our new method quantifies colocalisation in multi-wavelength datasets, relying on two steps. First, bright isotropic structures are detected in 3D in separate channels. After pruning, a matching procedure reveals the colocalisation distance between the objects in the different channels. As a model of study, we used first trimester trophoblast cell line JEG-3 and focused on the expression of histocompatibility class Ib antigens expressed at the trophoblast cell surface. The method is simple, robust and fast, producing superresolved distance maps using stringent criteria for colocalisation.

Materials and methods

Cell line and cell culture

The human placental choriocarcinoma cell line JEG-3 (kindly provided by Professor I.L. Sargent, Nuffield Department of Obstetrics and Gynaecology, University of Oxford, UK) was maintained in Dulbecco's Modified Eagle's Medium Ham's F-12 (PAA Laboratories GmbH, Austria), containing 10 % (v/v) fetal bovine serum (FBS) (PAA Laboratories GmbH, Austria). The cells were cultured at 37 °C in a humidified atmosphere of 5 % CO_2.

Immunofluorescence staining

It is important to use optimally stained samples for reliable image acquisition and analysis. Protocols are numerous and depend on sample and technique used. In our example, titration, washing and blocking steps for indirect immunofluorescence were optimised for the requisite antibodies and the choriocarcinoma cell line to exclude unspecific labelling. Various controls (cells only, cells labelled with

secondary antibody only, cells labelled with a secondary antibody unspecific for the primary antibody) are required to determine optimal protocol. Here, JEG-3 cells were seeded on coverslips or LabTek 8 well slides at a density of 8×10^3 cells per well and cultured for 2 days. The cells were then fixed with 4 % paraformaldehyde for 20 min on ice. All subsequent steps were carried out at room temperature. Cells were blocked with 2 % (w/v) bovine serum albumin (BSA) prepared in 1 × Phosphate buffered saline (PBS) for 1 h, then stained sequentially for each antigen by incubation with MEM-G/09 (anti-HLA-G) and MEM-E/07 (anti-HLA-E) (Exbio) monoclonal antibodies at a dilution of 2 µg/100 µl for 1 h at room temperature. Secondary antibody, anti-mouse IgG conjugated with Alexa Fluor 488 or Alexa Fluor 555 (Invitrogen, Carlsbad, CA, USA) was used at a dilution of 0.25 µg/100 ml for 1 h. Cell nuclei were stained with 4′,6-diamidino-2-phenylindole (DAPI) (Sigma Aldrich) diluted 1:250 in distilled water, then thoroughly washed and mounted with anti-fade mounting medium Vectashield (Vector Laboratories, Burlingame, CA, USA). A #1.5 coverslip was put on top and the edges sealed with rubber cement (Fixogum, Marabuwerke GmbH & Co., D-71732 Tamm, Germany).

Confocal microscopy

To reliably determine colocalisation with this method, it is important that optimised samples are acquired respecting several criteria. First, saturated pixels should be avoided, as they may represent lost information and cannot be used for quantification. Look-up tables (LUTs) colour-coding the maximum greyscale value are commonly implemented in microscope image acquisition software. This allows to detect saturated pixels and adjust laser power and/or detector gain to avoid them before the dataset is acquired. Second, datasets should be acquired with the correct sampling parameters. These are determined by the Nyquist–Shannon reconstruction theorem (Nyquist 1928; Shannon 1949). Briefly, this means that the smallest structure in an image, as determined by the microscope's resolution using Abbe's criterion, should be represented by at least two pixels. Higher sampling (three to four pixels) is also acceptable, but undersampling must be avoided. It also allows to remove single-pixel high-frequency noise through post-acquisition filtering (see below, "Image pre-processing"). Third, aberrations should be minimised in the imaging setup. This can be done using objectives corrected for spherical ('plan') and chromatic aberrations (achromatic, apochromatic and apochromatic violet-corrected (VC), depending on the number of colours corrected for). Furthermore, uni-, not bi-directional scanning, zooming into the centre of the field of view, and separating colours in line scanning rather than full-frame mode are good measures for minimising aberrations.

For image acquisition, a Nikon A1si confocal microscope was used with a plan-apochromatic VC1.4 N.A. 60× magnifying oil-immersion objective. Images were acquired in four channels, using one-way sequential line scans. DAPI was excited at 405 nm with laser power 3.2 arbitrary units (AU), and its emission collected at 450/50 nm with a PMT gain of 118 AU. Alexa Fluor 488 was excited at 488 nm with laser power 7.8 AU, its emission collected at 525/50 nm with a PMT gain of 140 AU (hereafter called the green channel). Alexa Fluor 555 signal was excited at 561 nm with laser power 2.1 AU, and collected at 595/50 nm with a PMT gain of 117 AU (hereafter called the red channel). Differential interference contrast images were acquired using the transmitted light detector at a gain of 103 AU. In all cases, no offset was used, and the scan speed was ¼ frames/s (galvano scanner). The pinhole size was 34.5 µm, approximating 1.2 times the Airy disk size of the 1.4 N.A. objective at 525 nm. Scanner zoom was centred on the optical axis and set to a lateral magnification of 55 nm/pixel. Axial step size was 140 nm, with 40–60 image planes per *z*-stack. Twelve cells with average to fair signal strength in both channels were examined. They were in isolated positions with few or no neighbouring cells, allowing accurate quantitation of the flat plasma membrane and uncrowded receptor distribution.

Image pre-processing

Once datasets have been acquired following the above guidelines, we recommend to apply PSF deconvolution before analysing them. Numerous approaches exist for measured or blind deconvolution of PSFs (Sibarita 2005; Biggs 2010; Model et al. 2011). If no such program is available, applying a simple 3D Gaussian smoothing filter is acceptable (Pawley 2006). Open source deconvolution software and Gaussian smoothing filters exist for ImageJ (Rasband 1997; Schneider et al. 2012) and its 'pre-packaged' version, Fiji (Schindelin et al. 2012). In our case, all datasets were deconvolved using AutoQuant X (version 2.2.1, Media Cybernetics, Inc., Bethesda, MD, USA) which is based on a combination of blind deconvolution (Ayers and Dainty 1988; Holmes et al. 2006) and maximum likelihood estimation (Holmes 1988; Holmes et al. 1995). In order to limit colocalisation analysis to a single cell, we traced its outlines using differential interference contrast and fluorescence images, excluding extracellular areas from analysis. Movement of the sample in *X* and *Y* direction while acquiring a *z*-stack, so-called stage drift, should also be corrected. Stacks can be aligned in one channel using the translational mode of the StackReg algorithm (Thévenaz et al. 1998) in ImageJ (Rasband 1997), and the

stored shift matrix applied to the other channel, since colour separation uses line scans, allowing for little deviation between the channels. Alignment can be validated by 3D visual inspection of PSFs in separate and fiduciary marks in overlaid channels.

Chromatic aberration correction

Chromatic aberration occurs because different wavelengths of light are focussed in different positions. While this can largely be corrected for in the objective, there are other sources (e.g. plane of coverslip not parallel to plane of microscope slide, refractive index mismatch, slight optical path misalignments). Open source programs (e.g. Kozubek and Matula 2000; Preibisch et al. 2010) and commercial software (e.g. Huygens Chromatic Shift Corrector, Scientific Volume Imaging, Hilversum, the Netherlands) exist to correct for these errors. We used polystyrene microspheres of 1.0 μm diameter (FluoSpheres® F-13082, Invitrogen, Carlsbad, CA, USA) that have excitation and emission spectra ideally suited for the two-colour setup used in this study. They were diluted to a concentration of 1:1000, sonicated, air-dried on a coverslip, embedded in Vectashield, sealed on a slide and imaged using the same acquisition parameters as for the cellular samples. The image stacks were then deconvolved and the bead centroids calculated. Vector fields showing the distances between one bead's centroid in the green and the red channel were analysed ($n = 837$ beads), and the average values in three dimensions used for translational shifting. The same shift was applied to colocalisation analysis of the receptors.

Colocalisation analysis

The colocalisation approach uses MATLAB software (version R2010b with Image Processing Toolbox; MathWorks Inc., Natick, Massachusetts) and is based on a 3D blob-like feature detection algorithm introduced by Obara and coworkers (2008). The workflow of the algorithm is depicted in Fig. 1. All steps are based on analysis in 3D. The algorithm is divided into two stages: candidate location detection and candidate location pruning. After acquisition of separate datasets for both receptors ('3D Image A and B'), the fluorescent intensity of particles is enhanced while suppressing the noise by convolving the image with a 3D Laplacian of Gaussian (LoG) kernel. The LoG kernel size is controlled by a user-defined radius r. Local maxima, detected by morphological opening, are then used to define all locations of particles brighter than their immediate surroundings. This process continues until a user-defined low intensity bound T (separate for each channel, to allow for datasets where noise levels are markedly different) is reached. This is the threshold below which no particles can be safely identified because of image noise. In order to accurately measure colocalisation of particles in the dual colour fluorescence images, their centroid positions were pinpointed at subpixel resolution using weighted centroids. A local matching procedure then performed an exhaustive search for correct matches between the two vectors of intersecting positions, using the expected average radius of the surrounding circle of light r. For each position in one channel, the Euclidean distance to every position in the other channel was calculated. Alternatively, a global matching procedure based on the Hungarian approach (Kuhn 1955) can be used here. If the distance of the closest pair is smaller than the maximum colocalisation distance d (also referred to as 'hard threshold'), then the pair is added to the list of matches and removed from the input vectors. All candidate locations are pruned to eliminate spurious locations due to image noise. The procedure is repeated until there are no more matches satisfying the maximum colocalisation distance condition. Receptor pairs with their centroids further apart than 165 nm were classified as non-colocalising. These remaining positions in both datasets are then labelled as unmatched.

The algorithm is available upon request from the corresponding authors.

Visualisation

After loading the program's Graphical User Interface (GUI) and a 3D dataset for each channel, the algorithm is run by pressing the 'Colocalisation' button. Results can then be viewed in five different ways: (1) Stacks: Centroid positions of all identified particles are marked by red dots in the image stacks, and sliders (in the 'Stacks' box of the GUI) allow to move through the different z-planes. To verify how exactly a superresolved centroid is positioned inside a fluorescent blob, a high zoom can be applied. (2) Maximum intensity projections: To visualise an entire dataset in one image, projections of each image stack are available ('Projection 1' and 'Projection 2' in the 'Plot' box), with green asterisks marking unmatched (non-colocalising) particles and blue circles indicating colocalisations. (3) Scatterplot: Produces an isometric perspective view of particles shown as asterisks (green and red for each channel), and colocalisations encircled in blue. The numbers for colocalisations and particles detected in each channel are also indicated. (4) Distance map: A colour-coded 3D distance map is used to visualise colocalisations. Each colocalisation is shown as a single sphere, with a coded colour indicating the distance between the two colocalising particles (Figs. 4, 5b). For accurate colour display, distances are grouped and colour-coded in five bins of 30 nm, ranging from 10 nm (blue end) to 170 nm

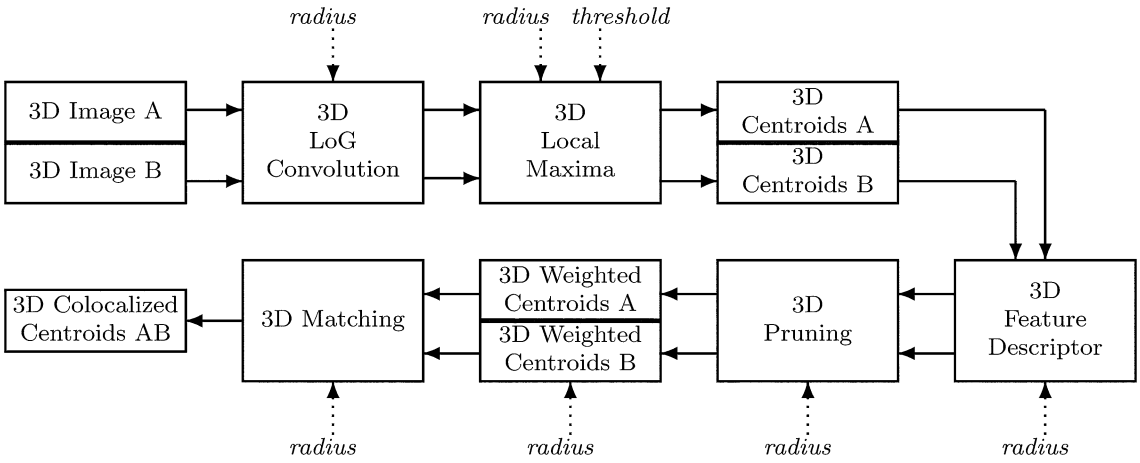

Fig. 1 Flowchart illustrating the main steps of the proposed approach. The *boxes* represent the main steps of the algorithm, while *dotted arrows* indicate user-defined parameters. 51 × 20 mm (600 × 600 DPI)

(orange end), shown as indicator bar on the right side of the produced figure. Binning is adapted to the user-defined maximum colocalisation distance. Images can be saved in standard formats. Note that scatterplots and distance maps are 3D and can be rotated within the figure window. (5) A histogram correlating the amount of colocalisations with the colocalisation distance can be produced to examine the distribution. Finally, the numerical results can be exported as a text file for further analysis.

For Fig. 3, the small region of interest from Fig. 2 was interpolated fivefold, and the greyscale images displayed with green and red look-up tables for the two channels to produce a raytraced volume projection. Surface rendered centroids were integrated in a composite view using NIS-Elements (version 3.21.03, build 705 LO) with advanced rendering settings.

Results

Confocal images of HLA-G and HLA-E receptors tagged with antibodies showed a multitude of round, blurred spots distributed over the surface of the cell. HLA-G and HLA-E surface receptors were visualised separately at different wavelengths, here called the green (HLA-G) and the red channel (HLA-E). The total amount of receptors varied considerably per cell, differing by an order of magnitude for both HLA-G (between 121 and 1102) and HLA-E (between 43 and 537) ($n = 12$, Sup. Mat. Table S1). Figure 2 shows a densely populated cell with 657 HLA-G (green) and 534 HLA-E receptors (red). The ratio of HLA-G to HLA-E remains similar in most cases. On average, there are twice as many HLA-G particles per cell compared to HLA-E (68 ± 14 % HLA-G, 32 ± 14 % HLA-E). At a maximum colocalisation distance of 165 nm, an average of 50 ± 24 % HLA-E receptors colocalise with HLA-G. As HLA-G receptors are twice as numerous, only 25 ± 17 % colocalise.

The antibody-labelled surface receptors appear as diffraction-limited isotropic spots of uniform size in each channel. As the resolution is poorer in the axial (z) direction than laterally (xy), the 3D appearance is cigar-shaped (Fig. 3). Applying the user-defined parameters of spot radius and level of background noise, the algorithm determines the centre of each ellipsoid, even if they vary considerably in fluorescent intensity and background noise. Two receptors (one from each channel) are then classified as colocalising if they do not exceed the user-defined parameter d—the maximum colocalisation distance between the centres.

Corrections for chromatic aberration augmented the number of colocalising particles by a further 8–14 %, as shown in Fig. 4. On average, colocalising particles were over 30 nm closer after correction. By zooming in close to the optical axis, spherical and chromatic aberrations were small and consistent. A global 3D translational shift was applied (43 nm in x, −53 nm in y, −13 nm in z-axis).

Sparse colocalisation can be identified using this method. As shown in Fig. 5, a cell with 236 HLA-G and 108 HLA-E receptors shows colocalisation of 76 HLA-G/HLA-E pairs using a maximum colocalisation distance of 165 nm.

Detection of sparse colocalisations was also tested using an artificial dataset (Table 1) in which only 4 of 100 particles colocalise. Increasing levels of noise were added. Our approach robustly identifies the four colocalisations, using identical parameters for all noise levels. At the highest noise level, only two false positives are identified in one channel. This compares favourably to the object-based method implemented in the popular ImageJ plugin

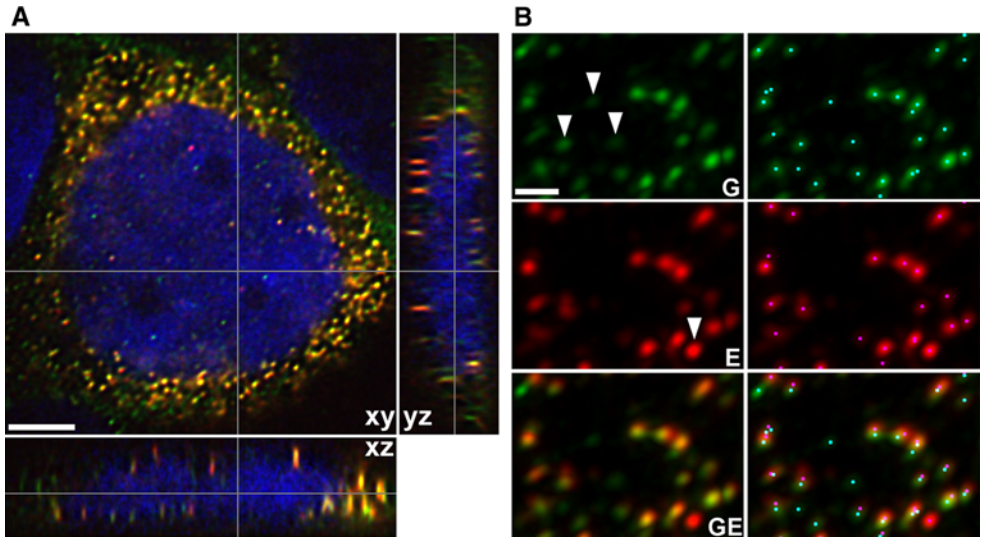

Fig. 2 JEG-3 trophoblast cell stained for HLA-G (*green*) and HLA-E (*red*). Colocalised receptors appear *yellow*. **a** Single-plane views of the cell in the *xy*, *yz* and *xz* direction. The cutting planes are indicated by the *grey horizontal and vertical lines*. *Scalebar* 5 μm. **b** *Left side* Magnified region of interest (projected in *z*) of HLA-G (*G*, *green*) and HLA-E (*E*, *red*) receptors, and their overlay (*GE*). Colocalising receptors appear *yellow*. *Arrowheads* mark unpaired receptors. *Right side* Same region with centroids marked in *cyan* for *G* and in *magenta* for *E*. *Scalebar* 1 μm. 129 × 63 mm (300 × 300 DPI)

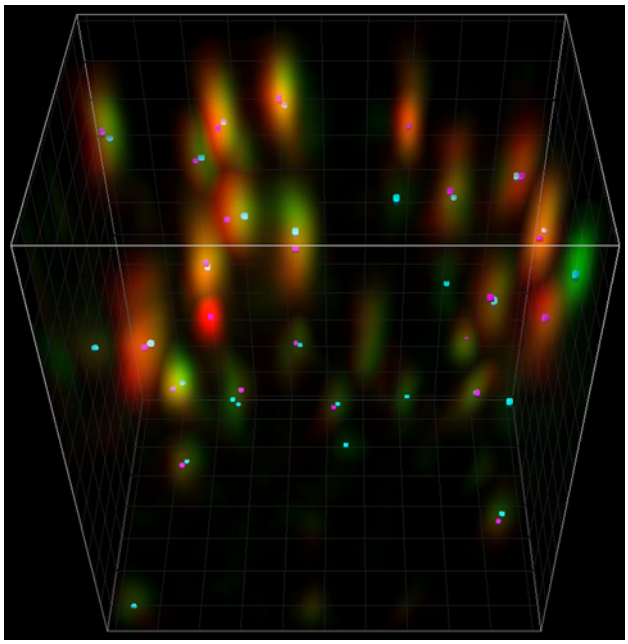

Fig. 3 Volume projection of a small area of spatially deconvolved HLA-G (*green*) and HLA-E (*red*) receptors. Many colocalise, while others are far apart (pair in *lower right corner*) or unpartnered (orphan *green* and *red* receptors). Centroids for HLA-G (*cyan*) and HLA-E (*magenta*) are rendered as small cylindrical surfaces. Grid size is 500 nm. 83 × 86 mm (300 × 300 DPI)

JaCoP (Bolte and Cordelières 2006). The accuracy of that approach drops markedly with increasing noise levels, despite adapting threshold values individually for each noise level to yield optimal results. The pixel-based correlation methods implemented in the same plugin—Manders's and Pearson's—yield coefficients which suggest non-colocalisation in both cases. These results show the disadvantages inherent in such pixel-based methods, as pointed out in the original study already (Bolte and Cordelières 2006).

Distances of colocalising receptors across the cells were pooled and a Weibull distribution curve fitted (Fig. 6a). This revealed a peak at 58 nm, indicating that this is the significant distance between antibody-labelled HLA-G and HLA-E receptors. We chose the point at which the curve flattens as cut-off point for the maximum colocalisation distance. This is 165 nm, at which point the third derivative of the curve crosses zero, indicating flattening (Sprott 2003).

To ensure that detected colocalisations were not due to random distribution of receptors on the cell surface, we tested the algorithm on randomised artificial datasets with similar PSF and SNR, but up to seven times more particles per channel than the biological specimens. Histogram analysis shows that particles in these dense, randomised datasets colocalise at much larger distances (Fig. 6b) than the biological ones (Fig. 6a). Relative colocalisation amounts were also compared (Fig. 6c), where colocalisations using a hard threshold of 360 nm were defined as 100 %. When decreasing this distance threshold in steps (165, 120, 80 and 40 nm), colocalisations in randomised datasets drop off sharply, while those of the biological specimens decrease significantly less. To ensure that these

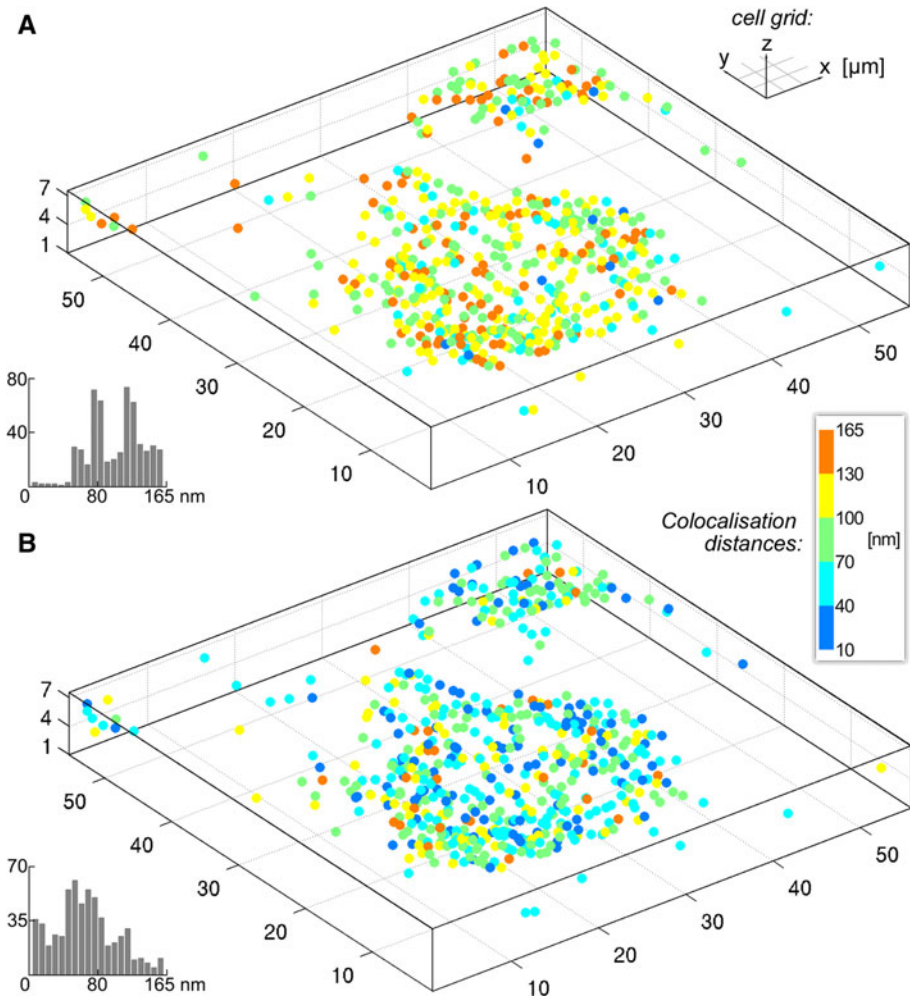

Fig. 4 Isometric 3D colour-coded scatterplots of Euclidean distances between colocalised HLA-G and HLA-E receptors on a JEG-3 cell (**a**) before and (**b**) after correction of chromatic aberration. Colocalisation distances range from 10 nm (*blue* end) to 165 nm (*orange* end), as indicated by the *bar* on the right side. Corresponding histograms are in the lower left corner of each scatterplot (abscissa: Euclidean distance of centroids, in nanometres; ordinate: number of colocalisations). Note that the grid for cellular dimensions uses microns. 129 × 140 mm (300 × 300 DPI)

controls were reproducible using parameters identical to those of the biological datasets, we applied the algorithm to biological datasets in which one channel was rotated by 90°. This allows the simulation of random colocalisations without altering the stochastic properties, PSF or SNR of the original dataset (Lachmanovich et al. 2003). Using the same hard threshold of 165 nm as in the original datasets, colocalisations in the randomised datasets lay between 1.7 and 2.2 %. This is significantly lower than the 14–77 % of receptor colocalisations found in this study.

Effects of the three user-defined parameters (Sup. Mat. Fig. S1A) were analysed. The parameters consist of particle radius, a background noise level for each channel and the maximum colocalisation distance. For a diffraction-limited spot, the radius can be determined by measuring the PSF, or by calculating the theoretical size, depending on the optical setup used. The default is set to 138 nm, the integer of 2.5 pixels of 55 nm length each, which also empirically proved a good starting point for most datasets. Applied to surface receptor datasets, the parameter is stable over a wide radial range (Sup. Mat. Fig. S1B). Values below 50 nm do not provide the algorithm with a large enough window to detect particles, and inaccuracies increase. Between 90 and 170 nm, the values are nearly constant, while at larger radii they start to decline. The noise threshold parameter was also found to be stable over a long range. In an artificial dataset (SNR 7.2, 100 colocalising particles), the number of spots is initially grossly overestimated, but entirely stable for normalised greyscale values from 0.3–0.7 (Sup. Mat. Fig. S1C). An artificial dataset in which the isotropic particles are increasingly removed from each other was used to show the behaviour of the maximum colocalisation distance. Unsurprisingly, the larger this distance, the more colocalisations are found (Sup. Mat. Fig. S1D). The distance between colocalisations can be calculated using either the Hungarian (Kuhn 1955) or Euclidean approach, but no differences were observed when user-defined parameters were set in the stable range.

Noise reduction using spatial deconvolution of the PSF changed the total amounts of detected particles and colocalisations. An example of a cell with high receptor count is shown before and after deconvolution (Sup. Mat. Fig. S1E),

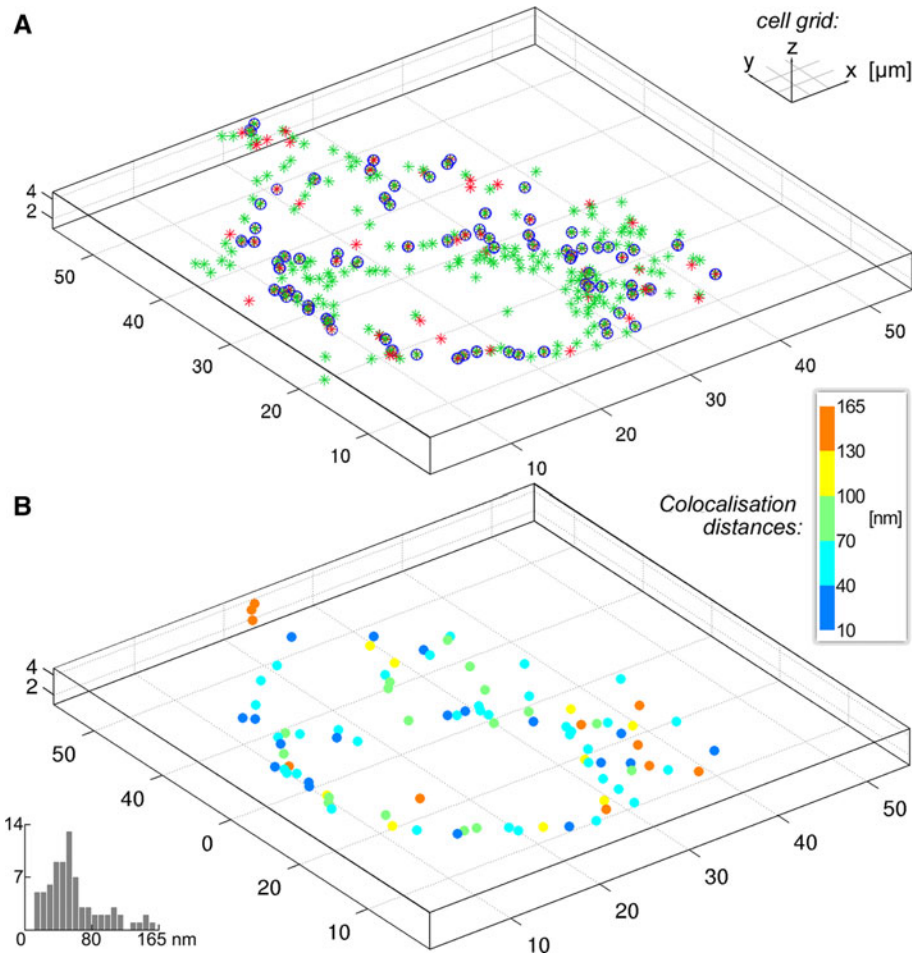

Fig. 5 Sparse colocalisation. **a** Isometric 3D colour-coded *scatterplot* of a single cell with HLA-G (*green asterisks*) and HLA-E receptors (*red asterisks*). Colocalising receptor pairs are demarcated by a *blue circle*. **b** Euclidean distance map of colocalised receptor pairs of HLA-G and HLA-E. Colocalisation distances range from 10 nm (*blue* end) to 165 nm (*orange* end), as indicated by the *bar* on the right side. The corresponding histogram is in the lower left corner of the scatterplot (abscissa: Euclidean distance of centroids, in nanometres; ordinate: number of colocalisations). Note that the grid for cellular dimensions uses microns. 129 × 131 mm (300 × 300 DPI)

Table 1 Analysis using artificial datasets of 100 particles, of which 4 colocalise

This study					JaCoP plugin (Bolte and Cordelières 2006)						
					Object-based				Manders		Pearson
	Particles		Coloc.		Particles		Coloc.				
SNR	R	G	True	False	R	G	True	False	R	G	
36	100	100	4	0	100	100	4	0	0.1	0.101	0.106
7.2	100	100	4	0	100	100	2	0	0.02	0.025	0.022
3.6	100	102	4	0	115	114	2	3	0.05	0.063	0.003

Different levels of noise are added, reducing the signal-to-noise ratio (*SNR*). Manders' and Pearson's correlation coefficients are given

Particles the number of detected particles in each channel (*R* for red channel, *G* for green channel), *Coloc* the number of measured colocalisations

with an increased percentage of detected particles in a single channel by 15 %, and by 6 % for colocalisations with particles in the other channel. High-frequency noise may also lead to detection of false positives, so deconvolution results in fewer particles and colocalisations. For results with high accuracy, it is thus recommended to restore images by spatial deconvolution (Landmann and Marbet 2004). High noise conditions were used in 3D test images to evaluate centroid localisation. The algorithm was able to reliably identify centroids at SNRs as low as 1.9 (Sup. Mat. Fig. S1F). Spot density was assessed for cells densely populated with isotropic structures, where spots in a single channel are likely to overlap partially. Particles very close to each other are recognised as separate if the distance between their centres are 1.2–1.6 times that of the particle's radius (Sup. Mat. Fig. S1 G). The algorithm was further

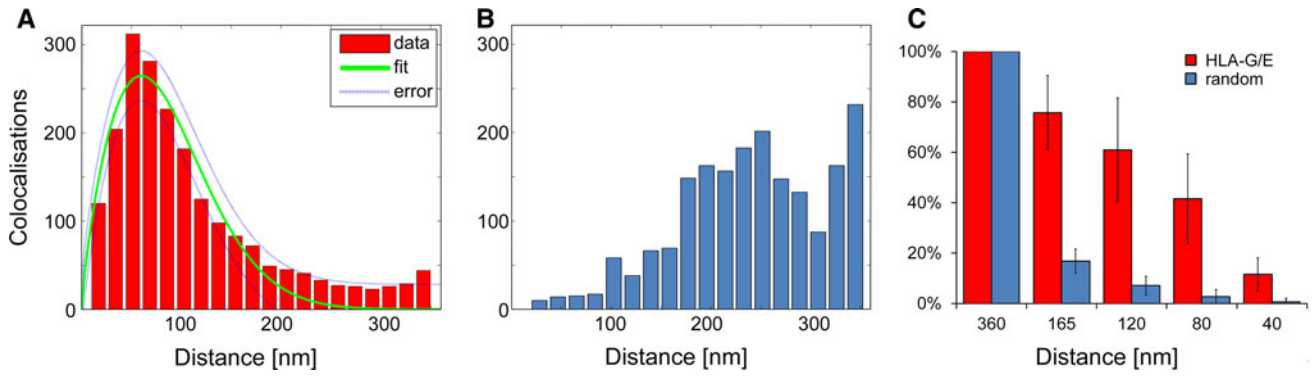

Fig. 6 Colocalisation distance histograms. **a** Colocalisation distances for HLA-G and HLA-E particles. The maximum is at 58 nm, and the curve flattens at 165 nm. **b** Colocalisation distances for randomised datasets with high density. **c** Comparison of relative colocalisation distances of HLA-G/HLA-E (*red*) and randomised samples (*blue*). Colocalisations with a hard threshold of 360 nm maximum colocalisation distance represent 100 %, then decreased in steps (165, 120, 80 and 40 nm). Error bars show standard deviation. 36 × 10 mm (600 × 600 DPI)

tested on other biological samples with isotropic structures. It reliably determined colocalisations in two-channel 3D datasets of double stainings for fungal actin patches (rhodamine-phalloidin and Cap1-GFP, Sup. Mat. Fig. S1H top), plant chloroplasts visualised by autofluorescence and labelled with a stromal GFP fusion (Sup. Mat. Fig. S1H middle) and rhodopsin-GFP aggresomes with a Golgi marker in mammalian HEK293 cells (Sup. Mat. Fig. S1H bottom). Finally, we have created a GUI (Sup. Mat. Fig. S1I) for ease of use.

Discussion

We present a simple, robust, superresolved and fast approach to quantify colocalisation of surface receptors. The main contribution of the algorithm lies in the overall methodology that is based on simple filtering operations followed by pruning stages that further refine the detection and localisation of the fluorescent particles' centres. Amount and distances between colocalising small isotropic spots or larger blobs were robustly identified in disparate datasets with varying fluorescent intensity and high background noise. For highest possible precision and accuracy of this approach, optimal image acquisition, correction of chromatic aberration and denoising of datasets are required. Following these steps, the dataset can be loaded and analysed using the GUI. Magnification indicates how many nanometres are covered by a single volume element (i.e. a pixel in all three dimensions). Default values are 55 nm in x and y and 140 nm in z, but depend on image size, zoom and z-step of the acquired dataset, and can usually be found in the dataset's metafile, or easily calculated. The user-defined parameters for colocalisation analysis can then be set. The average radius r of the isotropic particles in question should be indicated. This can be difficult to determine in datasets with low SNR, where the circle of light surrounding a fluorescent particle may be significantly corrupted by noise. However, the exact value only needs to be approximated, as the parameter is stable over a long range. Choosing a radius much larger than that of the particle will lead to longer computation times and fewer particles being detected. The noise threshold value T, ranging from 0 to 1, should be set between 0.1 and 0.9 for each channel separately. As with the radius, this parameter is stable over a considerable range. It is recommended to change parameters r and T (one at a time) to determine the stable range. This can be done by cropping a smaller part of the dataset for rapid checking of different values. Finally, the maximum colocalisation distance needs to be chosen. Where possible, this should be based on the size of the investigated isotropic structures. If this is unknown, the colocalisation distance histogram will show the distribution and may allow to infer the relevant range of colocalisation distances. Otherwise, it is arbitrary, and the higher the distance, the less likely particles are to truly interact. For results with high accuracy, we recommend to correct for chromatic aberration, stage drift (where required) and high-frequency noise. However, the algorithm has been applied successfully to datasets without any of these corrections, and may thus be used on uncorrected datasets to determine its suitability for the structures in question.

Our approach enables a weighting of the probability that two particles colocalise. The smaller the distance between two particles, the more likely they are to truly colocalise and interact. The distance map indicates this likelihood. Distances have been binned and colour-coded into five groups to show this clearly. We have further integrated a function that produces a histogram of all colocalisations and their distances. This enables the comparison of

distributions of sparse colocalisations with randomised ones, in absolute and relative ways. Importantly, it also allows to extract the significant spread of colocalisation distances. In our case, the 58 nm peak in the curve fitted to the pooled colocalisation distances can be explained by the size of HLA-G (Clements et al. 2005) labelled by two antibodies. With regards to our chosen hard threshold for colocalisations, it would seem unlikely that receptors 165 nm apart directly interact. However, it may well be that they are linked by adapter molecules, or have embarked on a lipid raft and are moving towards each other, as sizes of microdomains vary between 10 and 200 nm (Pike 2006).

Localisation accuracy of our method is limited by several factors. First, a main limitation is posed by the errors introduced during image acquisition. Sample preparation, image noise and the optical setup will invariably cause errors that can be minimised, but not fully eliminated. The error, best described by the standard deviation of perfectly colocalising fluorescent particles which emit light in both channels, was around 30 nm. Using fluorophores excited by the same laser, an accuracy of 10 nm has been reported (Lacoste et al. 2000), and closed-loop feedback control systems are capable of achieving subnanometre resolution (Pertsinidis et al. 2010). However, our approach is intended for use in standard research laboratories, which do not offer such technical options. Second, the accuracy of determining a centroid of an isotropic particle depends on the amount of photons collected by the imaging system (Thompson et al. 2002). Using SNRs above 2 and taking into account the margin of error in determining a centroid in three dimensions (Haralick and Shapiro 1992), measurement accuracy for our method is around 40 nm, agreeing with previous estimates for similar approaches (Schütz et al. 1998; Hess et al. 2007).

Pinpointing centroids of fluorescent particles using weighted centroids takes into account non-uniform distributions of fluorescent intensity. It has two further advantages. First, the procedure does not require interpolation of images: pixel-based interpolation leads to larger datasets. The higher the desired accuracy of subpixel-resolved centroid location, the larger the dataset, which inevitably requires more computing time. Second, when using weighted centroids, post-acquisition accuracy is theoretically only limited by the double precision floating-point calculations, which is much higher than that achievable by interpolation.

The code for this approach was not optimised for speed, but a deconvolved dataset was processed for an average of 3.8 min, including the application of cellular outline and translational shift, to determine superresolved colocalisation in 3D and produce the according figures. This algorithm has also performed well for datasets not subjected to deconvolution of the PSF. Thus, this approach could be used in a context where sparse colocalisations of punctate structures need to be identified with the analysed cell positioned for further measurements. For example, intensity-dependent or fluorescence-lifetime based FRET measurements of fixed cells, or slow-moving molecules tagged with fluorescent proteins, could corroborate protein–protein interaction of closely colocalising molecule pairs.

Expression of MHC class I molecules occurs during embryogenesis and at the fetomaternal interface (Cooper et al. 2007; Fernández et al. 1999). Here, we reveal colocalisation of the surface receptors HLA-G and HLA-E at an average intermolecular distance of 58 nm, suggesting interactions between these MHC class I molecules. In humans the most polymorphic class I molecules, HLA-A and B, are absent, and HLA-C has a diminished expression. What is intriguing is that the less polymorphic subset of class I molecules, also known as non-classical antigens HLA-E, HLA-F and HLA-G, are selectively expressed in syncytiotrophoblast tissue at the fetomaternal interface. It has been proposed that these molecules suppress or modulate the maternal immune system, protecting the embryo from a local inflammatory reaction and rejection (Ishitani et al. 2003; Rouas-Freiss et al. 1997); in particular, HLA-G is thought to deliver an inhibitory signal to NK cells, thus suppressing the maternal immune system from attacking the fetus. HLA-G has also been shown to be involved in oocyte implantation (Jurisicova et al. 1996). Dysregulation of HLA-G and any of the other non-classical class I antigens may lead to recurrent spontaneous abortions as it has been shown in IVF studies (Shaikly et al. 2008, 2010). The role of HLA-E and HLA-F is less clear and has not been studied in-depth. On a histological level, they have been shown to be differentially co-expressed (Ishitani et al. 2003). A high-resolution light microscopy study postulated that HLA-E may be regulated by colocalising with HLA-G (Shaikly et al. 2010). In that study, absolute amounts of receptor determined by flow cytometry are larger by an order of magnitude compared to values found here. But the relative ratio of HLA-G to HLA-E, with cells having on average twice as much HLA-G as HLA-E, is similar in both studies. It may thus be the ratio of HLA-G to HLA-E which is more important to immunomodulation than their absolute numbers per cell. The key question, however, remains how exactly these non-classical MHC class I receptors interact and regulate the function of trophoblast cells. Together with highly specific antibodies, appropriate cell lines and experimental conditions, the superresolved, stringent method for receptor count and colocalisation analysis presented here will allow to get closer to identify these regulatory mechanisms.

Acknowledgments We would like to thank the three anonymous reviewers for critical comments and pivotal suggestions, and J.A. Laissue, N. Kad and B. Amos for helpful discussions.

References

Anderson CM, Georgiou GN, Morrison IE, Stevenson GV, Cherry RJ (1992) Tracking of cell surface receptors by fluorescence digital imaging microscopy using a charge-coupled device camera. Low-density lipoprotein and influenza virus receptor mobility at 4 degrees C. J Cell Sci 101:415–425

Ayers GR, Dainty JC (1988) Iterative blind deconvolution method and its applications. Opt Lett 13:547

Biggs D (2010) 3D deconvolution microscopy. Curr Protoc Cytom, Chapter 12: Unit 12.19.1–20

Bolte S, Cordelières FP (2006) A guided tour into subcellular colocalization analysis in light microscopy. J Microsc 224:213–232

Clements CS, Kjer-Nielsen L, Kostenko L, Hoare HL, Dunstone MA, Moses E, Freed K, Brooks AG, Rossjohn J, McCluskey J (2005) Crystal structure of HLA-G: a nonclassical MHC class I molecule expressed at the fetal-maternal interface. Proc Natl Acad Sci USA 102(9):3360–3365

Cooper J, Dealtry G, Ahmed MA, Arck P, Klapp B, Blois S, Fernández N (2007) An impaired breeding phenotype in mice with a genetic deletion of beta-2 microglobulin and diminished MHC class I expression: role in reproductive fitness. Biol Reprod 77:274–279

Costes S, Daelemans D, Cho E, Dobbin Z, Pavlakis G, Lockett S (2004) Automatic and quantitative measurement of protein–protein colocalization in live cells. Biophys J 86:3993–4003

Fernández N, Cooper J, Sprinks M, AbdElrahman M, Fiszer D, Kurpisz M, Dealtry G (1999) A critical review of the role of the major histocompatibility complex in fertilization, preimplantation development and feto-maternal interactions. Hum Reprod update 5:234–248

Haralick R, Shapiro L (1992) Accuracy. Addison-Wesley Longman Publishing Co Inc., Chicago

Hess ST, Gould TJ, Gudheti MV, Maas SA, Mills KD, Zimmerberg J (2007) Dynamic clustered distribution of hemagglutinin resolved at 40 nm in living cell membranes discriminates between raft theories. Proc Natl Acad Sci USA 30(104(4)):17370–17375

Holmes T (1988) Maximum-likelihood image restoration adapted for noncoherent optical imaging. J Opt Soc Am A 5:666–673

Holmes TJ, Bhattacharyya S, Cooper JA, Hanzel D, Krishnamurthi V, Lin W, Roysam B, Szarowski DH, Turner JT (1995) Light Microscopic Images Reconstructed by Maximum Likelihood Deconvolution. In: Pawley J (ed) The handbook of biological confocal microscopy, 2nd edn. Plenum Press, New York, pp 389–402

Holmes TJ, Biggs D, Abu-Tarif A (2006) Blind deconvolution. In: Pawley J (ed) Handbook of biological confocal microscopy. Springer Science+Business Media LLC, NY, pp 468–487

Ishitani A, Sageshima N, Lee N, Dorofeeva N, Hatake K, Marquardt H, Geraghty DE (2003) Protein expression and peptide binding suggest unique and interacting functional roles for HLA-E, F, and G in maternal-placental immune recognition. J Immunol 171(3):1376–1384

Jurisicova A, Casper RF, MacLusky NJ, Mills GB, Librach CL (1996) HLA-G expression during preimplantation human embryo development. Proc Natl Acad Sci USA 93:161–165

Kozubek M, Matula P (2000) An efficient algorithm for measurement and correction of chromatic aberrations in fluorescence microscopy. J Microsc 200(Pt 3):206–217

Kuhn HW (1955) The Hungarian method for the assignment problem. Nav Res Logist 2(1–2):83–97

Lachmanovich E, Shvartsman DE, Malka Y, Botvin C, Henis YI, Weiss AM (2003) Co-localization analysis of complex formation among membrane proteins by computerized fluorescence microscopy: application to immunofluorescence co-patching studies. J Microsc 212:122–131

Lacoste TD, Michalet X, Pinaud F, Chemla DS, Alivisatos AP, Weiss S (2000) Ultrahigh-resolution multicolor colocalization of single fluorescent probes. Proc Natl Acad Sci USA 97:9461–9466

Landmann L, Marbet P (2004) Colocalization analysis yields superior results after image restoration. Microsc Res Tech 64(2):103–112

Li Q, Lau A, Morris T, Guo L, Fordyce C, Stanley E (2004) A syntaxin 1, Galpha(o), and N-type calcium channel complex at a presynaptic nerve terminal: analysis by quantitative immunocolocalization. J Neurosci 24:4070–4081

Malkusch S, Endesfelder U, Mondry J, Gelléri M, Verveer P, Heilemann M (2012) Coordinate-based colocalization analysis of single-molecule localization microscopy data. Histochem Cell Biol 137:1–10

Manders EM, Stap J, Brakenhoff GJ, van Driel R, Aten JA (1992) Dynamics of three-dimensional replication patterns during the S-phase, analysed by double labelling of DNA and confocal microscopy. J Cell Sci 103(Pt 3):857–862

Manders EMM, Verbeek FJ, Aten JA (1993) Measurement of co-localization of objects in dual-colour confocal images. J Microsc 169:375–382

Marquardt D (1963) An algorithm for least-squares estimation of nonlinear parameters. J Soc Ind Appl Math 11:431–441

Model MA, Fang J, Yuvaraj P, Chen Y, Zhang Newby B-MM (2011) 3D deconvolution of spherically aberrated images using commercial software. J Microsc 241(1):94–100

Morrison I, Karakikes I, Barber R, Fernández N, Cherry R (2003) Detecting and quantifying colocalization of cell surface molecules by single particle fluorescence imaging. Biophys J 85:4110–4121

Nyquist H (1928) Certain topics in telegraph transmission theory. Trans Am Inst Electr Eng 47:617–644

Obara B, Byun J, Fedorov D, Manjunath BS (2008) Automatic nuclei detection and dataflow in Bisquik system. Workshop on Bio-Image Informatics: Biological Imaging, Computer Vision and Data Mining. Santa Barbara

Pawley JB (2006) Points, pixels, and gray levels: digitizing image data. In: Pawley JB (ed) Handbook of biological confocal microscopy. Springer Science+Business Media LLC, NY, pp 59–79

Pertsinidis A, Zhang Y, Chu S (2010) Subnanometre single-molecule localization, registration and distance measurements. Nature 466:647–651

Pike LJ (2006) Rafts defined: a report on the keystone symposium on lipid rafts and cell function. J Lipid Res 47:1597–1598

Preibisch S, Saalfeld S, Schindelin J, Tomancak P (2010) Software for bead-based registration of selective plane illumination microscopy data. Nat Methods 7(6):418–419

Press W, Flannery B, Teukolsky S, Vetterling W (1992) Numerical recipes in C: the art of scientific computing, 2nd edn. Cambridge University Press, Cambridge

Rasband WS (1997) ImageJ. U. S. National Institutes of Health, Bethesda, Maryland

Rouas-Freiss N, Gonçalves R, Menier C, Dausset J, Carosella E (1997) Direct evidence to support the role of HLA-G in protecting the fetus from maternal uterine natural killer cytolysis. Proc Natl Acad Sci 94:11520–11525

Schindelin J, Arganda-Carreras I, Frise E, Kaynig V, Longair M, Pietzsch T, Preibisch S, Rueden C, Saalfeld S, Schmid B, Tinevez J-Y, White D, Hartenstein V, Eliceiri K, Tomancak P,

Cardona A (2012) Fiji: an open-source platform for biological-image analysis. Nat Methods 9:676–682

Schneider C, Rasband W, Eliceiri K (2012) NIH Image to ImageJ: 25 years of image analysis. Nat Methods 9:671–675

Schütz GJ, Trabesinger W, Schmidt T (1998) Direct observation of ligand colocalization on individual receptor molecules. Biophys J 74(5):2223–2226

Shaikly VR, Morrison IE, Taranissi M, Noble CV, Withey AD, Cherry RJ, Blois SM, Fernández N (2008) Analysis of HLA-G in maternal plasma, follicular fluid, and preimplantation embryos reveal an asymmetric pattern of expression. J Immunol 180(6): 4330–4337

Shaikly V, Shakhawat A, Withey A, Morrison I, Taranissi M, Dealtry G, Jabeen A, Cherry R, Fernández N (2010) Cell bio-imaging reveals co-expression of HLA-G and HLA-E in human preimplantation embryos. Reprod Biomed Online 20:223–233

Shannon CE (1949) Communication in the presence of noise. In: Proceedings of the IRE vol 37, pp 10–21

Sibarita JB (2005) Deconvolution microscopy. Adv Biochem Eng Biotechnol 95:201–243

Sprott JC (2003) Chaos and time-series analysis. Oxford University Press, Oxford

Thévenaz P, Ruttimann UE, Unser M (1998) A pyramid approach to subpixel registration based on intensity. IEEE Trans Image Process 7:27–41

Thompson R, Larson D, Webb W (2002) Precise nanometer localization analysis for individual fluorescent probes. Biophys J 82:2775–2783

Verveer PJ, Bastiaens PI (2008) Quantitative microscopy and systems biology: seeing the whole picture. Histochem Cell Biol 130(5):833–843

Wolter S, Schüttpelz M, Tscherepanow M, Van de Linde S, Heilemann M, Sauer M (2010) Real-time computation of subdiffraction-resolution fluorescence images. J Microsc 237: 12–22

Zinchuk V, Zinchuk O, Okada T (2007) Quantitative colocalization analysis of multicolor confocal immunofluorescence microscopy images: pushing pixels to explore biological phenomena. Acta Histochem Cytochem 40:101–111

	Number of receptors		*Colocalisations at hard threshold of:*				
Cell	HLA-G	HLA-E	360nm	**165nm**	120nm	80nm	40nm
1	121	168	53	47	38	30	6
2	236	108	87	76	72	57	21
3	282	177	70	53	48	34	9
4	644	520	202	149	121	74	19
5	657	534	454	411	371	273	88
6	900	537	450	395	353	260	79
7	1102	514	164	72	45	19	4
8	451	43	39	31	18	10	3
9	560	156	60	30	11	8	1
10	837	264	213	163	135	82	19
11	633	140	119	89	74	49	15
12	469	165	136	109	96	59	14
Average	*574*	*277*	*171*	*135*	*115*	*80*	*23*
Stdev	*286*	*191*	*143*	*132*	*121*	*90*	*29*

Table S1 *Number of detected receptors and their colocalisations, depending on the maximum colocalisation distance ('hard threshold'). Stdev = Standard deviation, n=12.*

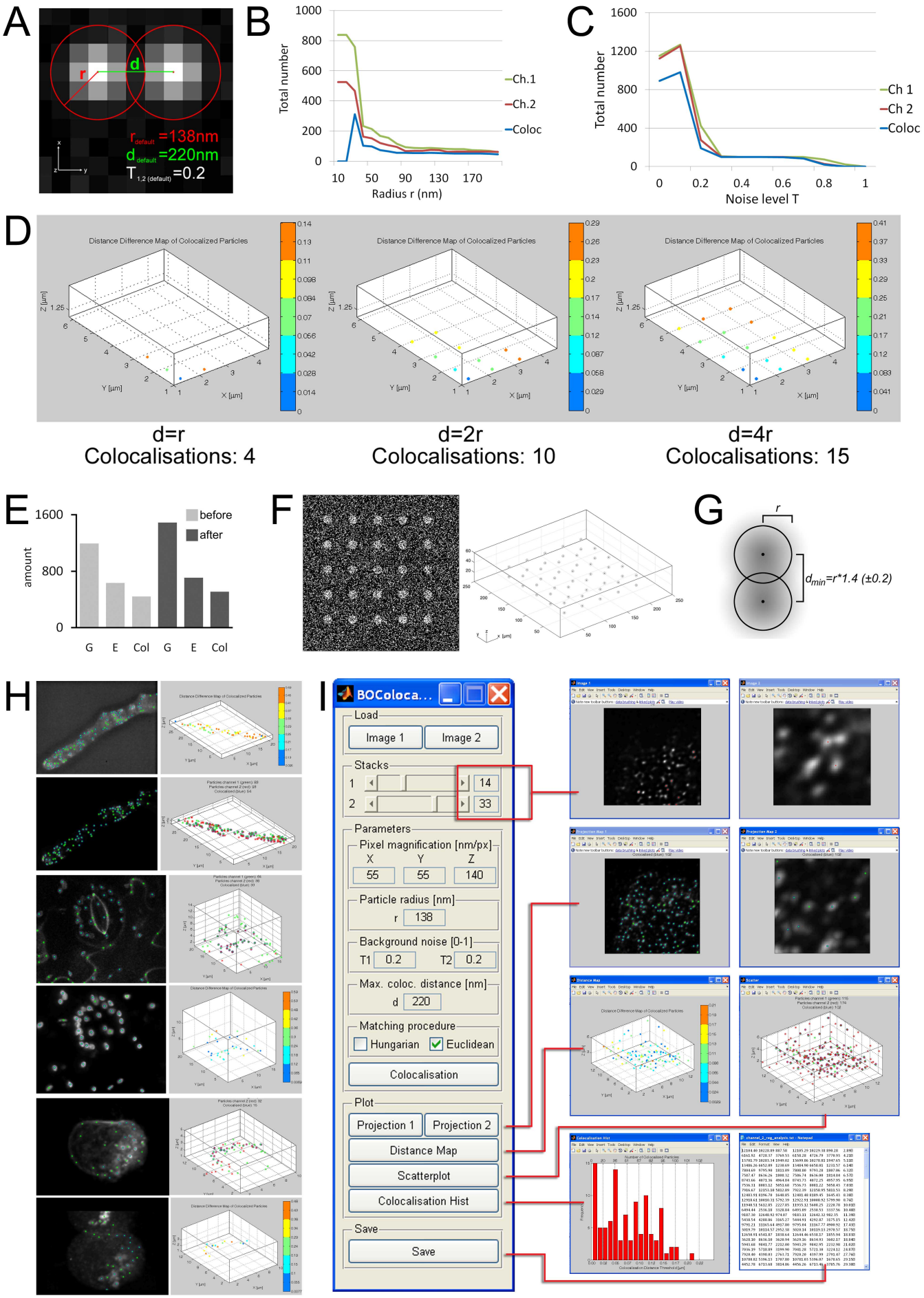

Supplemental Material, Fig. S1 **A)** Depiction of the parameters used for assessing colocalisation, indicated with their default values. **B)** Effect of varying particle radius on number of detected particles and colocalisations. *Ch.1 = Channel 1, Ch.2 = Channel 2.* **C)** Effect of varying noise level on number of detected particles and colocalisations. **D)** Effect of varying maximum colocalisation distance on number of detected particles and colocalisations. **E)** Effect of deconvolution on number of detected particles and colocalisations. **F)** Robust detection of blob-like structures and their centres at low signal-to-noise ratio. **G)** Illustration of spot density as function of radius. Note that this applies only to dense spots in one single channel. **H)** Detection of isometric particles in disparate datasets. Top: Fungal actin patches labelled with capping protein (Cap1-GFP) and rhodamine-phalloidin. Middle: Plant chloroplasts visualised with YFP and autofluorescence. Bottom: HEK293S cells with rhodopsin-GFP aggresomes and Golgi marker. **I)** Screenshot of Graphical User Interface (GUI), showing analysis flow from top to bottom. The GUI is on the left side, the output on the right side. For functions of both channels (*Stacks* and *Projection*), the second is zoomed into.